Chapter 4

Hydrogen order-disorder transition in metal (II) hydroxides

4.1 Introduction

The family of metal hydroxide, $M(OH)_2$ (M= Mg, Ni, Co, Fe, Cd and Mn), have a trigonal structure with space group P-3m1 and consists of layers of MO_6 octahedra as shown in Fig. 4.1. The interlayer spacing is occupied by hydroxyl groups directed along the stacking direction of MO_6 octahedra where each hydroxyl group (O-H) lies in the vicinity of three oppositely oriented O-H group of the neighbouring layer. This configuration gives rise to two parallel planes of hydrogen atoms adjacent to each other. At ambient condition, the distance between nearest hydrogen atoms, i.e, the H--H distance for $Mg(OH)_2$, β-$Co(OH)_2$, β-$Ni(OH)_2$ is 2.198, 2.199 and 1.92 Å respectively which is less than the Pauli's van der Waals separation (2.4 Å) [107]. When subjected to compression, the interlayer separation of MO_6 layers decreases, and hence reduces the H--H distance thereby leading to an increase in repulsive force between two hydrogen atoms. Since the H--H repulsive force cannot rise indefinitely under compression, it destabilizes the initial sublattice of hydrogen atoms and the symmetry of the lattice. Hence, a structural transition involving changes in hydrogen sublattice is expected in all these isostructural metal hydroxides under compression. High-pressure study on these compounds showed that, under pressure, the protons are displaced from the $2d$ site to one of the three $6i$

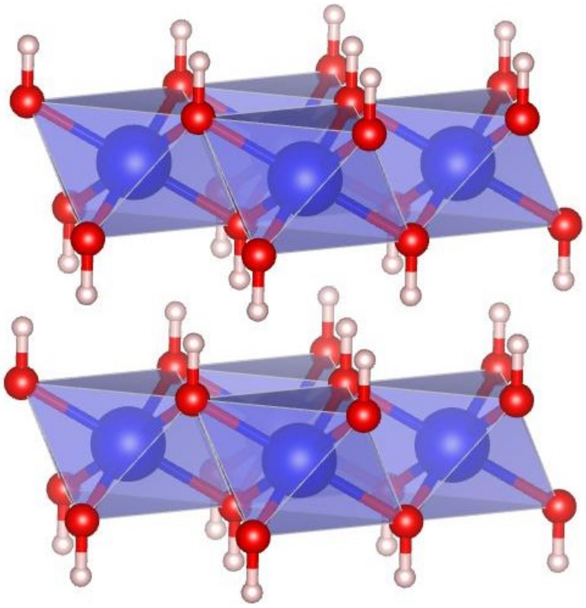

Figure 4.1: Crystal structure of $M(OH)_2$ (M= Mg, Ni, Co, Fe, Cd and Mn) with layers of MO_6 octahedra. Blue, grey and red spheres represent metal, oxygen and hydrogen atoms respectively.

$(x, \bar{x}, z)$ Wyckoff positions having equal occupation [108] resulting in hydrogen disordered phase. The hydrogen disordered model lacks mirror symmetry owing to displaced proton from the $2d$ site thereby reducing the initial symmetry of the lattice from P-$3m1$ to P-3. However, the transition of hydrogen ordered to disordered structure is debated in these compounds particularly for the widely studied brucite mineral where the determination of its ground state structure at ambient condition is under question. Literature survey of $Mg(OH)_2$, β-$Co(OH)_2$ and β-$Ni(OH)_2$ highlighting lack of systematic investigation in providing a consistent picture of hydrogen order-disorder transition from both theoretical and experimental point of view is presented in Sections 4.3, 4.4 and 4.5 respectively.

In this work, the compression behaviour of three minerals $Mg(OH)_2$, β-$Co(OH)_2$ and β-$Ni(OH)_2$ as reference candidates from the $M(OH)_2$ family of compounds have been studied using combined synchrotron X-ray powder diffraction (XRPD) and density functional theory (DFT) based first principles calculations with the main focus on the behaviour of hydrogen atoms in these minerals and to seek a common characteristic of these isostructural compounds under compression.

4.2 Methodology

4.2.1 Computational methods

The theoretical evaluation of structural properties of $Mg(OH)_2$, β-$Co(OH)_2$ and β-$Ni(OH)_2$ at ambient and high-pressures were done by performing DFT based first principles calculations using Quantum Espresso code [90, 91]. The initial structure of $M(OH)_2$ (M=Mg, Co, Ni) for ambient condition was modelled from the brucite structure reported in the literature [109] with hydrogen at ordered site (P-3m1: space group No. 164). Since there are known failures of DFT in describing transition metal oxides due to self-repulsion and the missing derivative discontinuity in the exchange-correlation functional leading to over delocalization of electrons, we employed DFT+U approach [110] in calculations for β-$Co(OH)_2$ and β-$Ni(OH)_2$. The value of U (=4 eV) for these compounds was adopted from literature. To incorporate hydrogen disorderness at high-pressure, a $\sqrt{3} \times \sqrt{3} \times 1$ supercell was adopted which was proposed by Mookherjee, and Stixrude [111] to study disordering of hydrogen atoms in brucite. The valence and core electrons were represented by Projector Augmented Wave (PAW) [66] pseudopotentials. To account the van der Waals (vdW) forces in the layered configuration of these compounds, vdW-dF2 functional [112] was employed. The **k**-grid of dimension 10×10×10 and energy cut-off of 110 and 140 Ry for truncating the plane wave were chosen for unit-cell and $\sqrt{3} \times \sqrt{3} \times 1$ supercell respectively after performing a series of convergence test for $Mg(OH)_2$, β-$Co(OH)_2$ and β-$Ni(OH)_2$. Structural relaxation at various pressures was performed employing Broyden–Fletcher–Goldfarb–Shanno (BFGS) algorithm [93] and internal stress were computed [113–117]. The convergence threshold of total energy and force was set to 10^{-8} Ry and 10^{-4} eV/Å respectively. The ambient pressure lattice parameters were calculated with and without the inclusion of vdW in order to estimate the effect of vdW (Ref Table 4.4 of Section 4.4.1). Even though the inclusion of U parameter improves the electronic properties [118], the chosen value underestimates the lattice parameters, on the other hand, inclusion of vdW functional improves the lattice parameters close to experimental value with 0.07% deviation in c/a ratio with that of experimental value as shown in (Ref Table 4.4 of Section 4.4.1). Further, structural optimization of $Mg(OH)_2$, β-$Co(OH)_2$ and β-$Ni(OH)_2$ was tested using: 1) PBEsol, PBE, LDA (without including van der Waal (vdW) forces), 2) Inclusion of vdW interaction using semi-empirical DFT-D approach (LDA+D, PBE+D3, LDA+D3, PBE+D3) and 3) Inclusion of vdW interaction using non-empirical vdW functional (vdW-DF2) methods. Consistent symmetry of relaxed structures where obtained when the vdW interaction was treated with vdw-DF2 functional during optimization of both unit cell and supercell having initial symmetry of P-3m1 and P-3 respectively, suggesting vdw-DF2 functional as the better candidate for high-pressure study of these compounds. The pressure dependent charge distribution along lattice planes defined by hydrogen atoms were calculated and analysed using VESTA software [119] which calculates electron densities by the Fourier transform of structure factors from atomic scattering factors and structure parameters. VESTA was also used for structural illustration purpose in this thesis. Calculation of elastic constants were performed by evaluating the stress tensor corresponding to a set of strains. Numerical derivatives of stress with respect to strain were obtained using thermo_pw code implimented within the Quantum Espresso package. The phonon frequencies of brucite were calculated employing the Density Functional Perturbation Theory (DFPT) [94] on 8×8×8 mesh of **q**-points.

4.2.2 Experimental methods

Samples of $Mg(OH)_2$, β-$Co(OH)_2$ and β-$Ni(OH)_2$ having high purity from Sigma Aldrich were used in this work. XRPD measurements of $Mg(OH)_2$ at low temperatures and β-$Ni(OH)_2$ at ambient condition were carried out at the X-ray diffraction beamline (XRD1) of the Elettra Sincrotrone, Trieste with photon wavelength of 0.7 Å. The diffraction data were collected using a Pilatus2M 2-dimensional detector. The integration of two-dimensional powder pattern were done using Fit2D program following the callibaration of hardware using LaB_6 filled capillary serving as standard refrence powder (NIST-660a). A cryocooler system of Oxford Cryostream700 A was used for temperature dependent measurements of $Mg(OH)_2$. High-pressure synchrotron XRPD measurements of β-$Co(OH)_2$ and β-$Ni(OH)_2$ were performed at the Xpress beamline of Elettra Sincrotrone, Trieste [78, 120] having synchrotron radiation with monochromatic wavelength of 0.4957 Å and beam diameter of 40 micron. High-pressure XRPD measurements were performed on powders filled in a capillary of quartz with inner diameter of 100 microns. A membrane DAC with diamonds having culet size of 500 microns were used to apply the pressure. The sample chamber was prepared by pre-indenting a steel gasket of 200-micon thickness to about 80 microns and a hole having a diameter of 160 micron was prepared at the centre. An automatic membrane pressure drive was used to apply the pressure. 20% of the volume of sample chamber where occupied by pressed pellets of the sample, and the rest of the chamber were filled by the pressure transmitting medium (PTM). The in-situ monitoring of pressure was done by measuring the fluorescence of ruby chips having diameter in range of 5-20 micron placed within the sample chamber. An automatic membrane pressure drive was used to apply pressure. The pressure stability on the samples where ensured by measuring ruby fluorescence successively before the collection of actual data in addition to the given time interval between two successive pressure values. Two independent high-pressure runs were carried on β-$Co(OH)_2$ and β-Ni(OH), first using 4:1 methanol:ethanol mixture and second with silicone oil (SO) as PTM. The high-pressure data were collected using a MAR345 imaging plate detector. The accumulation time for diffraction was 180 s and 60 s for 4:1 methanol-ethanol mixture and SO run respectively. Rietveld refinements of diffraction patterns for obtaining the structural parameters were carried out using the Fullprof package. XRPD data were collected at smaller pressure intervals inorder to ensure sufficient data for β-$Co(OH)_2$ and β-$Ni(OH)_2$ in the low pressure regime.

4.3 Brucite under volume perturbation

The crystal structure of brucite ($Mg(OH)_2$) was first reported by Zigan, and Rothbauer [121] with hydroxyl group lying parallel to the three-fold axis with hydrogen atoms at $2d$ Wyckoff position (1/3,2/3,z). Duffy et al. [122], in their initial study on brucite, observed new Raman bands near 410 cm^{-1} and suggested transition of brucite from P-3m1 to a lower symmetric structure above 1.1 GPa owing to hydrogen rearrangement. However, in their later study [123], the hydrogen order-disorder transition in $Mg(OH)_2$ was shown to occur at 4-5 GPa. Higher transition pressure was determined by Catti et al. [124] from neutron diffraction study where they showed that the brucite in P-3m1 symmetry is stable up to 10.9 GPa beyond which its structure is described by a hydrogen disordered XGT model. However, no further studies to date has been reported for such high stability limit of brucite in P-$3m1$ symmetry. In contrast, a neutron diffraction measurement by Desgranges et al. [108] suggested hydrogen disordered structure for brucite even at ambient pressure. This indicates that the neutron diffraction measurement, which is a promising technique for determining hydrogen position, fails to provide a consistent picture of crystal symmetry of brucite, particularly the preferred hydrogen sites at ambient condition. This led to a wide range of subsequent experimental and theoretical investigation for determining the proton behaviour in brucite under pressure. Neutron diffraction study was carried by Chakoumakos et al. [125] to investigate the changes in crystal structure of brucite under thermal contraction. Their data yield better fit with the three-site model indicating that a hydrogen disordered structure is preferred for brucite throughout the studied temperature range, and was further re-confirmed from their later study [126]. However, the direction of the O-D bond initially remained closer to the c-axis whereas on further lowering the temperature below 100 K, the O-D bond deviated from the c-axis suggesting that the displacement of hydrogen atom is sensitive towards volume compression. A re-investigation on proton behaviour in brucite under low temperature using neutron powder diffraction study [127] showed that the thermal contraction under which hydrogen order-disorder transition occurs corresponds to the pressure value of 1.5 GPa. However, they didn't acquire any data points between 0 and 1.5 GPa, which insists us to investigate the hydrogen disordering in brucite at pressure lower than 1.5 GPa.

Several theoretical studies have also been reported on high-pressure study of brucite, however, less effort has been invested to probe the hydrogen order-disorder transition. The first two theoretical work on brucite using Hartree-Fock LCAO formalism didn't consider the disordered model for brucite [128, 129]. Pressure driven hydrogen order-disorder transition in brucite was reported by Raugei et al. [130] using molecular dynamics simulation. A detailed investigation using first principles calculations considering both hydrogen ordered and disordered model for brucite was performed by Mookherjee, and Stixrude [111] where the hydrogen disordered structure with P-3 symmetry (XLT, XGT arrangement) was modelled using $\sqrt{3}\times\sqrt{3}\times 1$ supercell. Among the two possible XLT and XGT arrangement, they showed that XLT arrangement is unfavourable since hydrogen retained the $2d$ site during structural relaxation. However, no such observation was reported structural relaxation of XGT arrangement, rather its energy values were close to that of P-3m1 symmetric structure. Hence, the study couldn't provide the conclusive evidence for the symmetry of brucite in its ground state symmetry, though, it was shown that the P-3m1 is favourable at large volumes. Since the estimated volume at ambient pressure may vary with the approximated form of exchange-correlation potential used, the interpretation of ground state structure at 0 GPa from the estimate of volume is not satisfactory. They concluded that the brucite undergoes a pressure-induced transition from nearly ordered hydrogen positions to dynamically disordered state followed by a static disordered structure. Previous experimental investigation on brucite showed that the interlayer bonding in brucite is characterized by the weak dispersive forces between the layers [108, 123, 124, 131–133], hence the inclusion of weak forces in DFT based calculation of brucite is inevitable. Ugliengo et al. [134] considered the dispersive interaction in their calculation through an empirical correction to DFT energy for studying structural and vibrational properties of brucite in P-3m1 symmetric unit cell. Further, they didn't considered the hydrogen disordered model. An indirect indication used for reporting the transition of hydrogen ordered to disordered state in brucite was the anomalous behaviour of its elastic constants with pressure [135]. DFT and molecular dynamics study by Jochym et al. [136] suggested that the brucite exhibits P-3 symmetric structure at 0 GPa owing to discrepancies in elastic constants calculated for P-3m1 symmetric brucite with that of experiments whereas elastic constant calculated for P-3 symmetric brucite yield good agreement with reported experimental data. However, they didn't report displacement of hydrogen atom to the 2d site during the process of structural optimization of P-3 symmetric unit cell. The favoured P-3 symmetry for brucite at 0 GPa from elastic constants was later discarded by Pishtshev et al. [137] where they obtained a better agreement of calculated elastic constant with that of experimental results from P-3m1 symmetric brucite. Interestingly, a very recent density functional theory based study by Treviño et al. [138] showed that the symmetry of brucite at 0 GPa and 0 K is neither P-3m1 nor P-3, rather it has monoclinic symmetry with space group $C2/m$. Their conclusion was based on the phonon dispersion calculations where they obtained imaginary frequency modes at **K** symmetry point and along the **Γ-A** path of the Brillouin zone for P-3m1 and P-3 symmetric unit cell of brucite respectively whereas real phonon frequencies were obtained for $C2/m$ symmetric brucite. They further showed that the imaginary phonon modes of P-3 symmetric brucite turn real at 300 K, however, it failed to reproduce the experimental Raman spectrum. Therefore they concluded that the brucite exhibits $C2/m$ symmetry at 0 GPa in the temperature range 0-600 K. It is to be noted that their calculation didn't considered inclusion of vdW interaction, further, they didn't reported displacement of hydrogen atom from $6i$ to $2d$ sites during the process of structural optimization of P-3 symmetric unit cell of brucite.

Even though it is widely accepted that the brucite prefers hydrogen disordered structure under pressure, ambiguity exists on determining the favourable atomic site for hydrogen atom of brucite at 0 GPa. Independent theoretical study favours P-3m1 [137], P-3 [136] and $C2/m$ [138] symmetries for brucite at ambient conditions. Further, the hydrogen order-disorder transition pressure is still unclear as hydrogen disordered structure is even reported for the ambient condition [136]. One contributing factor to these observed discrepancies is that hydrogen disordering in brucite is sensitive to small volume change. Hence, to investigate the ground state structure and structural changes in brucite under small volume compression, we performed a combined density functional theory based first principles calculations, taking into account the inclusion of vdW interaction, hydrogen disorderness, and low temperature XRPD study, wherein the latter case, volume compression is achieved through the thermal contraction.

4.3.1 Results and Discussion

We initially investigated the ground state symmetric structure of brucite at 0 GPa. Both hydrogen ordered and disordered structures of brucite were reported as competing candidates, however, the conventional unit cell of brucite with P-3m1 symmetry cannot model the dynamically disordered hydrogen sublattice in a static calculation. Therefore, a $\sqrt{3} \times \sqrt{3} \times 1$ supercell model proposed by Mookherjee, and Stixrude [111], which can either have P-3m1 or P-3 symmetry depending on the optimized position of hydrogen atom is used. Fig. 4.2 shows the relation between P-3 and P-3m1 unit cell.

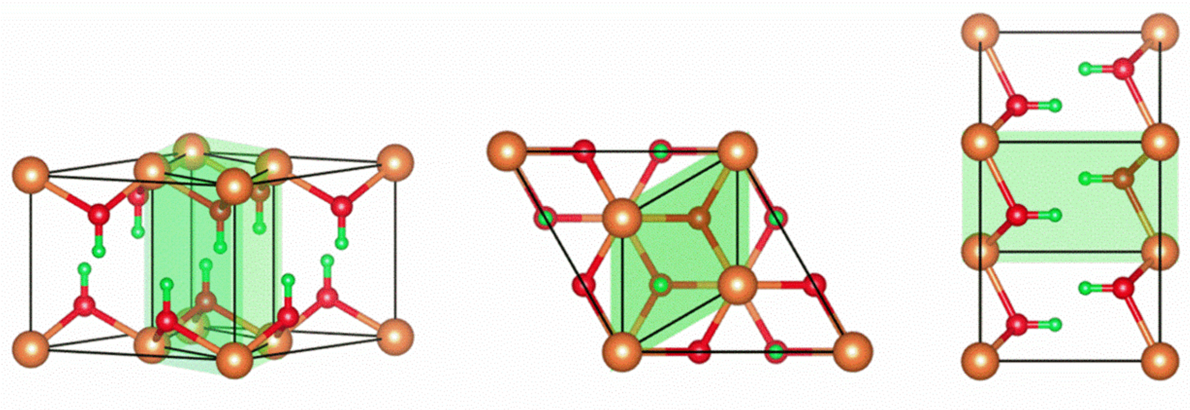

Figure 4.2: Relation between $\sqrt{3} \times \sqrt{3} \times 1$ supercell model and ideal P-3m1 (in green highlight) structure in different orientations.

Their lattice parameter are related as a_{sc}=a_c/*2cos(30)* where a_{sc} and $a_c$are the lattice parameter of $\sqrt{3} \times \sqrt{3} \times 1$ supercell and conventional unit cell respectively. The Mg atoms occupy 1a (0,0,0) and 2d (1/3,2/3,z) Wyckoff sites and the hydrogen and oxygen atoms occupy 6g sites with fractional coordinates (x,$2x$,z). Among the proposed XLT : (x,$2x$,z); $x < 1/3$ and XGT :(x,$2x$,z); $x > 1/3$ configuration [126, 131, 139–141], XLT arrangement was shown to be energetically unfavourable as the hydrogen atoms were displaced to 2d sites during structural relaxation [111]. Hence, in this work, geometrical relaxation on P-3 symmetric $\sqrt{3} \times \sqrt{3} \times 1$ supercell with XGT arrangement was performed. Since P-3 is a maximal subgroup of P-3m1 and the only symmetry operation that switches between these two space group is one mirror symmetry, the $\sqrt{3} \times \sqrt{3} \times 1$ supercell enables switching between P-3 and P-3m1 symmetry during structural relaxation yielding the ground state configuration of the unit cell. A similar approach was used by Mitev et al. [142], however, they performed constrained geometrical optimization by fixing the position of Mg atoms and constraining the x,y degrees of freedom for the oxygen atom.

The structural relaxation in this study were carried out using both non-empirical vdW functionals and semi-empirical DFT-D approach starting from a disordered supercell of brucite with P-3 symmetry. Treatment with non-empirical vdW functionals showed that hydrogen atom is unstable at 6i sites at 0 GPa where the hydrogen atoms relaxed back to 2d sites from its initial geometry during the relaxation process. The symmetry of the relaxed geometry was P-3m1 as determined from the FINDSYM online algorithm [143]. The geometry optimization provides a straightforward conclusion that P-3m1 symmetry is

Table 4.1: Lattice parameters and volume of $Mg(OH)_2$ obtained from XRPD measurements and DFT calculations using vdw-DF2 functional.

a (Å)	c(Å)	c/a	V(Å^3)	Method	Ref.
3.146	4.770	1.516	40.890	XRD (300 K)	This work
3.186	4.848	1.522	42.611	vdW-DF2	This work
3.188	4.786	1.501	42.120	PBEsol	[138]

favourable over P-3 symmetry in brucite. However, such transition from hydrogen ordered to disordered structure during structural optimization was not observed while using semi empirical or by excluding vdW interaction, which justifies the structural optimization results of previous DFT study [144]. The structural parameters of brucite at 0 GPa is shown in Table 4.1. Our measured and calculated lattice parameters using P-3m1 are consistent with those reported in literature. The calculated phonon dispersion curves yield real frequencies along the high symmetry directions of the Brillouin zone, as shown in Fig. 4.3, which confirms the lattice dynamical stability of P-3m1 symmetric structure of brucite. This is in contradiction with the results of Treviño et al. [138] where they obtained imaginary modes for P-3m1 symmetric structure at the **K** point which might be an artifact of numerical inaccuracy or the choice for treating exchange-correlation

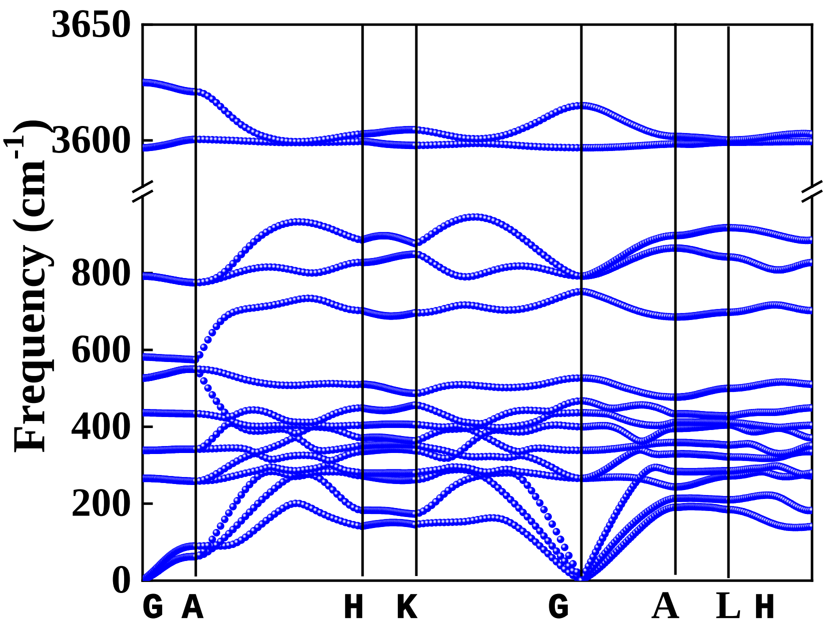

Figure 4.3: Phonon dispersion curves of brucite calculated using P-3m1 unit cell at 0 GPa

functional. We further validate the ground state structure of brucite from zone centre vibrational mode and elastic constants' calculations, as their agreement with experimental results often served as the factor for accepting the 0 GPa structure for brucite [136, 144]. The measured Raman spectrum of brucite is shown in Fig. 4.4. The calculated positions of vibrational modes using P-3m1 symmetric structure is marked by sticks in Fig. 4.4. All observed Raman modes detected in our experiment were observed in DFT calculation and is tabulated in Table. 4.2. A good agreement with the calculated and measured frequencies validate the hydrogen ordered structure for brucite at 0 GPa. The calculated elastic modulii, elastic constants and sound velocities of brucite in P-3m1 symmetric structure are shown in Table 4.3. The elastic constants are in good agreement with available experimental data, further, it follows Born stability criteria for the trigonal system given by Equation (4.1) thereby confirming the mechanical stability of P-3m1 symmetric structure of brucite at 0 GPa. We attribute the discrepancy reported for the elastic constants of P-3m1 symmetric structure by Jochym et al. [136] to their choice of

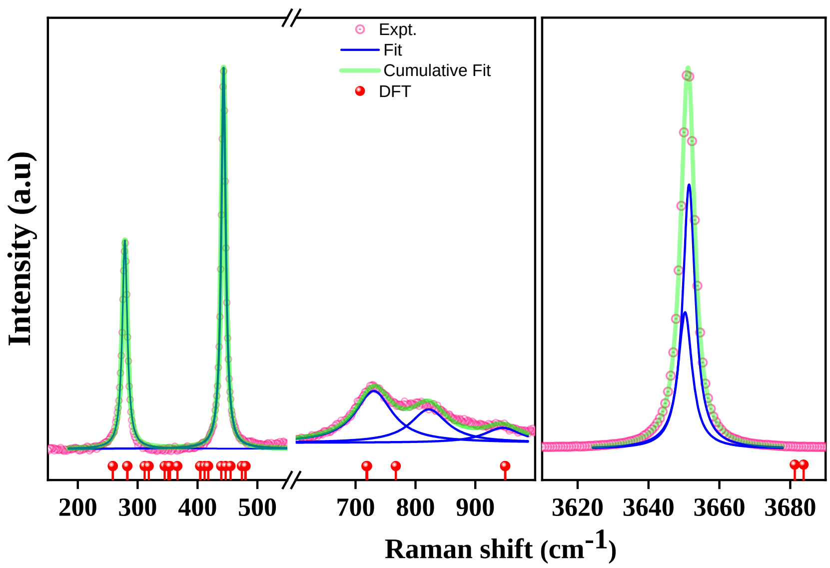

Figure 4.4: Raman spectrum of brucite measured at ambient condition using Raman spectrometer of Xpress beamline at Elettra. (For clarity, low and high frequency Raman modes are presented using different scales.). Calculated position of Raman modes using DFT is respresented using sticks

Table 4.2: Experimentally measured and DFT calculated frequencies (in cm^{-1}) of brucite in comparison with the available theoretical and experimental data.

Modes	This work		Ref. [138]	Expt. [145]	Ref. [146]	Ref. [147]	Ref. [148]
	DFT	Expt.					
R	256 ($2A_g$)	278.53	267.6 (E_g)	280	278	268	281
I	285 ($2A_u$)						
R	311.6 (A_g)						
R	318.7 (A_g)						
I	343 (A_u)						
R	352 (A_g)						
I	354 (A_u)		352.2 (E_u)	361	364	349	375
I	359 ($2A_u$)					375	
R	366.3 (A_u)						
R	412 ($2A_g$)						
I	417.9 (A_g)		462.2 (E_u)	416	459	422	399
I	422 (A_u)						
R	439.5 (A_g)	443.5	435.2 (A_{1g})	443	454	449	449
I	446.5 (A_u)						
I	447.1 (A_u)		471.1 (A_{2u})	461	499	487	495
I	455 (A_u)						
I	474.0 (A_u)						
I						600	
R	718 ($2A_g$)	732.43					
I	719 ($2A_u$)						
R	767 ($2A_g$)	822.47	786.3 (E_g)	725	803	767	798
R	949.9 (A_g)	945.77					
I	950.2 (A_u)						
R	3680.2 (A_g)	3650.33	3726.8 (E_g)	3652	3847	3686	3770
R	3682.0 ($2A_g$)	3651.46					
I	3681.7 (A_u)						
I	3697.1 (A_u)		3769.3 (A_{2u})	3688	3873	3727	3813

Table 4.3: Elastic constants, elastic modulus (GPa), and sound wave velocites (shear and longitudinal in km s^{-1}) of brucite at 0 GPa. The calculated values are compared with reported data. (*Calculation performed on *P*-3 unit cell. V, R and VHR denotes Voigt, Reuss and the Voigt–Reuss–Hill average, respectively)

Elastic parameters	This work	Expt. [149]	Expt. [150]	DFT* [137]	DFT [144]	Deformation Theory. [135]
C_{11}	148.8	154.0	156.7	130.6	192.9	156.7
C_{12}	40.4	42.1	44.4	70.3	50.5	51.3
C_{13}	9.9	7.8	12.0	10.0	11.7	24.5
C_{14}	0.0	1.3	0.2	-	2.8	9.8
C_{33}	47.5	49.7	46.3	48.5	67.2	21.6
C_{44}	18.7	21.3	21.7	20.4	29.9	24.4
B_R	32.7	51.2	36.7	-	66.7	-
B_V	51.0	43.8	55.2	-	48.6	-
B_{VHR}	41.9	31.3	-	-	57.7	-
G_R	27.1	36.4	30.4	-	51.5	-
G_V	36.8	39.1	39.3	-	41.6	-
G_{VHR}	32.0	-	-	-	46.6	-
V_P	6.2	6.3	6.7	-	7.1	-
V_S	3.8	4.2	4.1	-	4.4	-

exchange-correlation potential.

$$\begin{aligned} B_1 &= C_{11} - |C_{12}| > 0 \\ B_2 &= (C_{11} + C_{12})\, C_{33} - 2\left|C_{13}^2\right| > 0 \\ B_3 &= (C_{11} - C_{12})\, C_{44} - 2\left|C_{14}^2\right| > 0 \end{aligned} \tag{4.1}$$

The difference in Reuss and Voigt bounds of elastic modulus in Table. 4.3 is due to the strong anisotropy exhibited by the elastic constants. C_{11}, which corresponds to the strength along the *a*-*b* plane is thrice to that of C_{33}, which corresponds to strength along the *c* direction. This is expected as the interlayer separation is governed by weak dispersive forces. More detailed analysis on elastic properties of brucite in the *P*-3*m*1 structure has been reported in Ref. [135, 144, 149]. Following the promising result from the structural

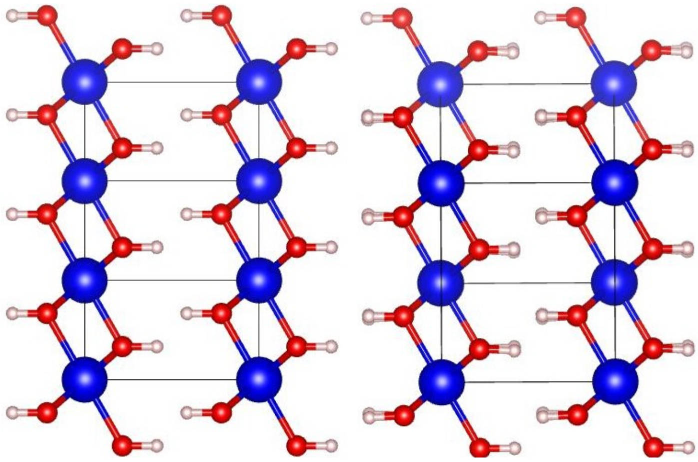

(a) (b)

Figure 4.5: Optimized geometry of brucite at 0 and 0.3 GPa after structural relaxation of $\sqrt{3} \times \sqrt{3} \times 1$ as starting model using vdw-DF2 functional.

relaxation of $\sqrt{3} \times \sqrt{3} \times 1$ super-cell at 0 GPa, we investigated the dependence of hydrogen sublattice under small volume compression by applying an external pressure of 0.5 GPa in intervals of 0.1 GPa. Figure 4.5 shows the optimised crystal structure of brucite at 0 and 0.3 GPa which corresponds to small volume compression. The hydrogen atom relaxes back to $2d$ sites up to 0.2 GPa, beyond which hydrogen remains at the disordered position, i.e; brucite undergoes P-3m1 to P-3 transition at 0.3 GPa. The results show that the preferred site for the hydrogen atom is sensitive to compressive volume perturbation.

To verify the observed changes in structure of brucite under volume compression experimentally, we performed XRPD study at low temperatures in range 110-400 K where the compression of volume is achieved through thermal contraction. The ambient condition XRPD data refined using P-3m1 and P-3 model are shown in Fig. 4.6(a) and (b) respectively. The structural parameters obtained from the refinement is presented in Table 4.1 along with the calculated and reported parameters which show reasonable agreement with each other. However, both P-3m1 and P-3 models yield good fitting of the data indicating that the XRPD data couldn't confirm the symmetry of the brucite structure at 0 GPa. Here, P-3m1 model was chosen for refining the low temperature XRPD data and the changes in the diffraction pattern of brucite at low temperatures were analysed with reference to Bragg peaks indexed at 300 K. The change in compressibility of lattice parameter with temperature is shown in Fig. 4.7. The c parameter is more

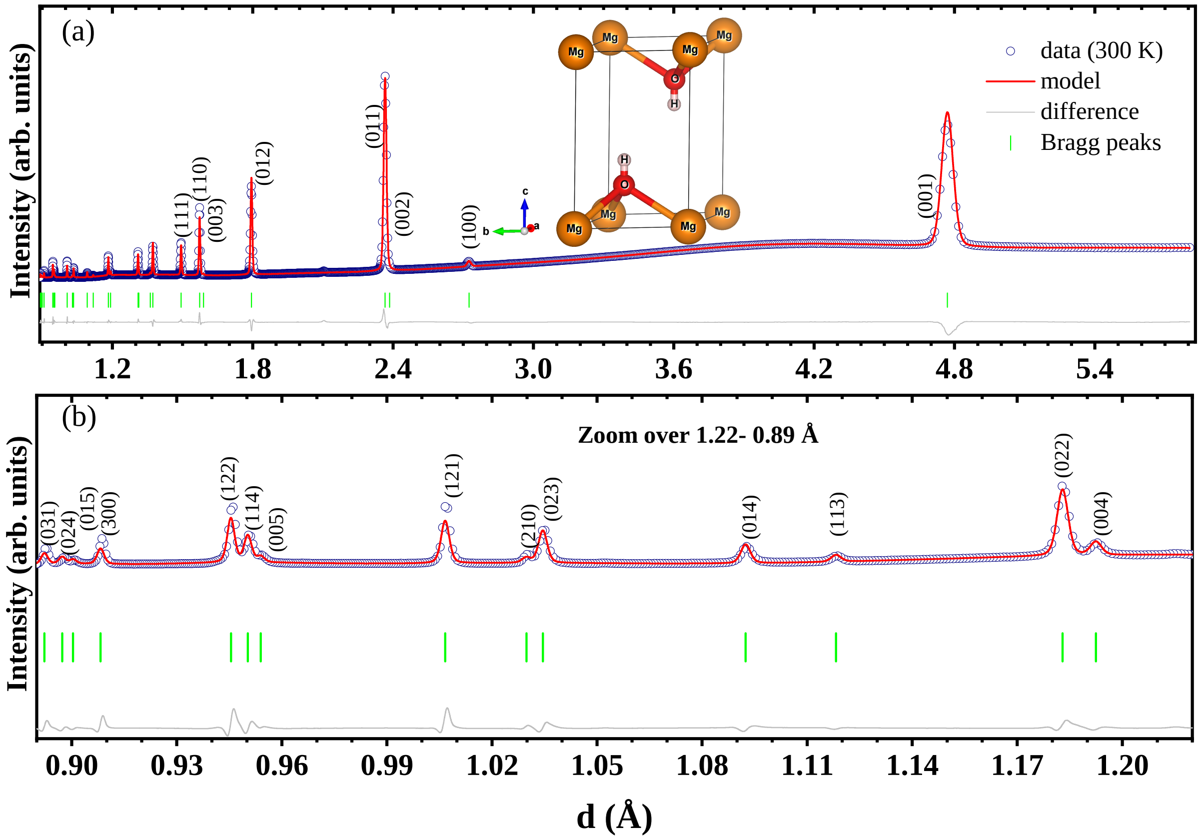

Figure 4.6: (a) Rietveld refinement of XRPD data of $Mg(OH)_2$ at 300 K using P-3m1 symmetric unit cell (see inset). Red solid lines and circles represents calculated patterns and measured data respectively. Bragg peak positions are indicated in green vertical bars. (b) A zoomed view of 0.9 – 1.22 Å which shows good fit between the XRPD data and refinement using P-3m1 unit cell.

compressible than the lattice parameter a as temperature decreases. The anisotropic behaviour of brucite is due to the interlayer separation of MgO_6 octahedra characterized by the weak vdW interaction as compared to the strong covalent interaction along a-b plane. This behaviour is identical to the high-pressure behaviour of brucite reported in the literature which shows the equivalent effect of thermal contraction and external pressure on the layered structure of brucite. Preliminary analysis of diffraction pattern of brucite in temperature range 100-400 K shows that the Bragg peaks such as (001) and (100) peaks characterizing the lattice parameters behave without showing any characteristics of structural phase transition as shown in Fig. 4.8. However, careful analysis of the XRPD data shows that few of the low intense Bragg peaks such as (015), (114), (005), and (013) show anomalous behaviour with a decrease in temperature as shown in Fig. 4.8, where their d-spacing decreases faster as compared to other main peaks and merges with the

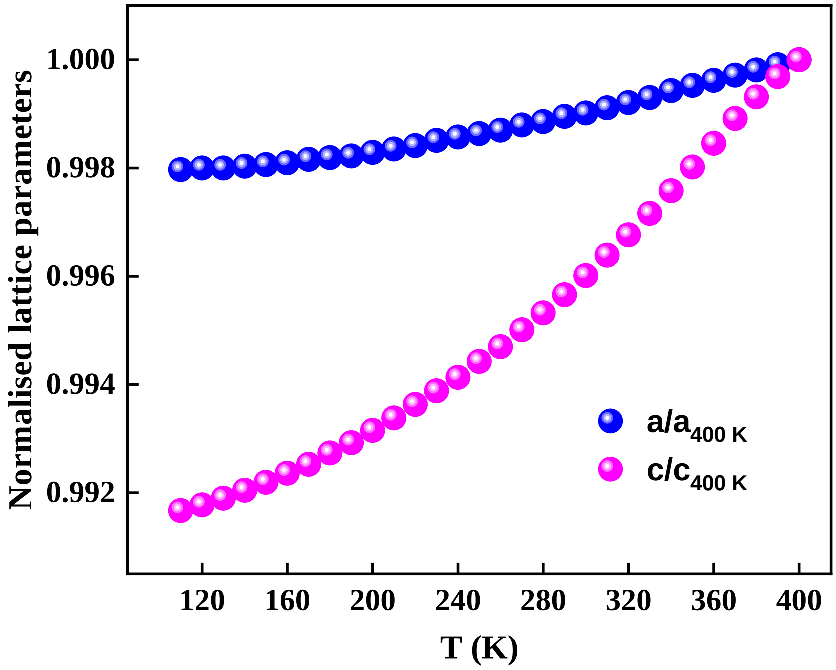

Figure 4.7: Normalised lattice parameters of brucite with temperature.

neighbouring peaks at a temperature near to 150 K. The behaviour of these peaks can be explained by investigating the lattice planes corresponding to these reflections and the results obtained from DFT calculations.

The lattice planes corresponding to the (001), (100), (015), (114), (005), and (013) peaks are shown in Fig. 4.9. The charge distribution along these planes are governed by the arrangement of O and H sublattice for (015) and (114) peaks, and H sublattice for (005) and (013) peaks. The charge density distribution along (100) and (001) planes is governed by the arrangement of Mg atoms. The normal behaviour of (001) and (100) peaks shows that the underlying symmetry of Mg sublattice is preserved consistent with the theoretical calculations, while, the anomalous behaviour of (015), (114), (005), and (013) Bragg peaks are attributed to the rearrangement of hydrogen atoms at temperature below 150 K. The stress arising due to thermal contraction within the structure at a temperature of 110 K is equivalent to effective pressure of ∼0.2 GPa. Therefore, the disordering of hydrogen atoms in brucite at lower temperature corroborate with our results from first principles calculations that shows a hydrogen order-disorder transition at 0.3 GPa. The one-to-one correspondence between anomalous behaviour of Bragg peaks corresponding to hydrogen sublattice under thermal contraction and P-3m1 to P-3 transition disorder

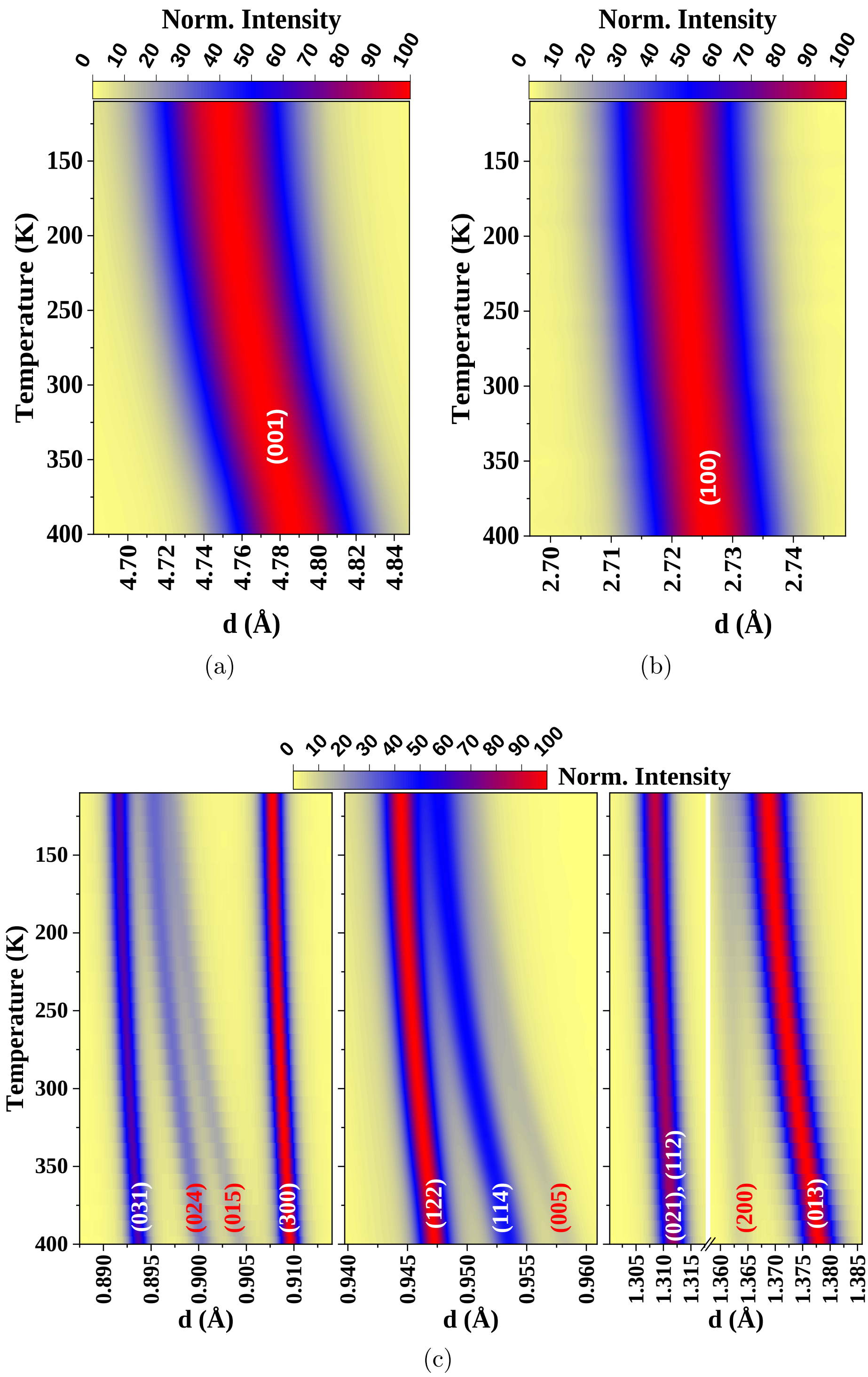

Figure 4.8: Intensity profile and interplanar spacing (d) of (a) (001), (b) (100) and (c) the anomalously behaving(015), (114) and (005) Bragg peak.

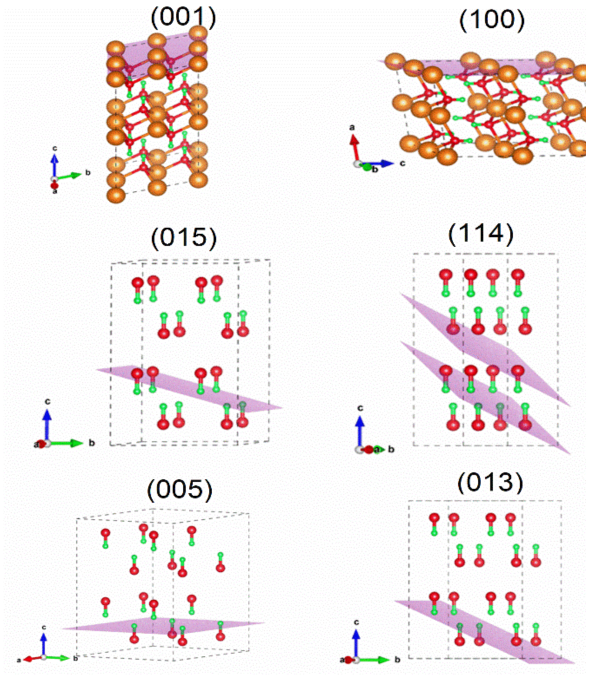

Figure 4.9: The crystallographic planes corresponding to (001), (100), (015), (114), (005) and (013) peaks.

under small volume compression attribute the observed Bragg peak anomaly to hydrogen disordering in brucite under compressive volume perturbation. Further, the study shows that hydrogen disordering in brucite is sensitive to volume compression such that the pressure generated by thermal contraction was sufficient to displace the hydrogen atoms from their ideal $2d$ sites to $6i$ sites.

We further report the volume and linear thermal expansion coefficient (TEC) of brucite at low temperatures. Very first reports on thermal expansion of brucite was published by Redfern, and Wood [151] for the temperature range 20 - 310 $^\circ$C which was later modified by including low temperature data points by Chakoumakos et al. [125]. The reported values for the instantaneous TEC at 0 K are $\alpha_a = 9.26 \times 10^{-6}\mathrm{K}^{-1}, \alpha_c = 3.77 \times 10^{-5}\mathrm{K}^{-1}$ and $\alpha_{\mathrm{vol}} = 5.73 \times 10^{-3}\mathrm{K}^{-1}$. Polynomial fitting of our measured lattice parameter with respect to temperature for brucite yield the following quadratic relations:

$$\begin{aligned} a &= 3.1424(1) - 2.1(9) \times 10^{-6} T + 4.9(2) \times 10^{-8} T^2 \\ c &= 4.7469(4) - 1.5(3) \times 10^{-5} T + 3.06(6) \times 10^{-7} T^2 \\ V &= 40.596(5) - 1.9(4) \times 10^{-4} T + 3.91(9) \times 10^{-6} T^2 \end{aligned} \tag{4.2}$$

The instantaneous isobaric thermal expansion can be obtained by differentiating Equation (4.2) as $1/x_0(\partial x/\partial T)_p$ where x_0 is a reference lattice constant at T_0. Fig. 4.10(a) presents the TEC (α) of brucite as a function of temperature. Thermal expansion in minerals is often described in averaged values of TEC. The mean TEC is given as $\bar{\alpha_x} = 1/x_0(\Delta x/\Delta T)$. The mean thermal expansion coefficient of brucite obtained from our low temperature data are:

$$\bar{\alpha}_a = \bar{\alpha}_b = 7.0229 \times 10^{-6} K^1$$

$$\bar{\alpha}_c = 2.9107 \times 10^{-5} K^{-1}$$

$$\bar{\alpha}_V = 4.3294 \times 10^{-5} K^{-1}$$

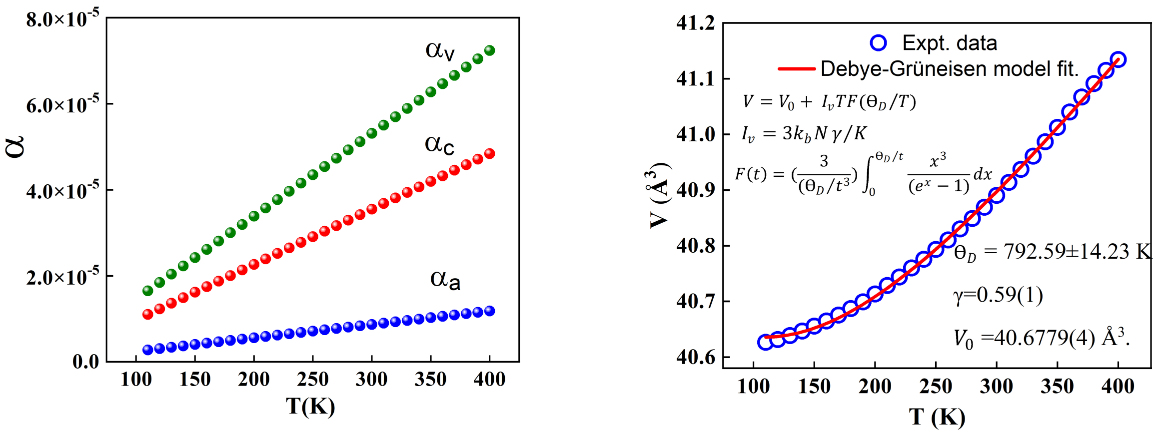

(a) (b)

Figure 4.10: (a) TEC of brucite with temperature. (b) Fitting of V-T data with Equation (4.3).

Following Debye-Grüneisen approximation, the description of lattice thermal expansion enables in defining the volume vs temperature curve using few important parameters such as Grüneisen parameter (γ), Debye temperature (θ_{D}) and the volume (V_0) extrapolated at 0 K and is given by Equation (4.3) [152]

$$V = V_0 + I_v T F(\frac{\theta_{\mathrm{D}}}{\mathrm{T}}) \tag{4.3}$$

with $F(t) = \frac{3}{\Theta_D/t^3} \int_0^{\theta_D/t} \frac{x^3}{e^x-1} dx$, $I_v = 3k_b N\gamma/K$, where N, K and k_b are the number of atoms per unit cell, bulk modulus and Boltzmann constant respectively. The temperature dependence of unit-cell volume was fitted using the method of least-square fitting formulated by Sayetat et al. [152] for determining θ_D and γ as shown in Fig. 4.10(b). This model describes the behaviour of anisotropic hexagonal systems for temperature values greater than $\theta_D/10$. Using the value of bulk modulus calculated from DFT calculations, the least square fitting yielded the values: $\theta_D = 792.59 \pm 14.23K$, $\gamma = 0.59(1)$ and $V_0 = 40.6779(4)\text{Å}^3$.

4.4 Hydrogen order-disorder transition in β-$Co(OH)_2$

Pressure induced structural changes similar to brucite were also reported for β-$Co(OH)_2$. The reported vibrational spectroscopic study on β-$Co(OH)_2$ showed that the infrared (IR) peak corresponding to O-H stretching mode exhibits broadening at 11 GPa [153] similar to $Ca(OH)_2$ [132]. In case of $Ca(OH)_2$, the broadening of O-H stretching mode were accompanied by loss of X-ray diffraction peaks suggesting pressure induced amorphization in $Ca(OH)_2$, however, no such signs of pressure induced amorphization were observed in the diffraction pattern of β-$Co(OH)_2$ at high pressures [153]. Therefore the observed broadening of IR stretching mode of O-H was attributed to amorphization of hydrogen sublattice in β-$Co(OH)_2$. Neutron diffraction study on attributed the anomalies in IR and Raman spectra of β-$Co(OH)_2$ to H--H repulsion induced structural frustration [140]. All these studies showed that the β-$Co(OH)_2$ undergoes hydrogen sublattice structural changes above 10 GPa. However, a recent study on pressure dependence of Raman spectrum of β-$Co(OH)_2$ by Marini et al. [154] reported an anomaly in full width at half maximum (FWHM) of modes associated with O-H bond of β-$Co(OH)_2$ at a pressure around 2 GPa. However, there are no other studies in the literature that reports structural anomaly in β-$Co(OH)_2$ at such low pressures. One of the reasons could be the subtle nature of such transition that, if exists, can be only detected by incorporating sufficient number of experimental data points with smaller pressure intervals in the low-pressure regime. With reference to the Raman spectroscopic evidence of structural anomaly in β-$Co(OH)_2$ at low pressure, we studied the structural response of β-$Co(OH)_2$ up to 7 GPa using combined synchrotron XRPD measurement and DFT based first principles calculations. The behaviour of Bragg peaks with pressure was analysed and the results were corroborated with that from DFT calculations.

4.4.1 Results and Discussion

The XRPD data of β-$Co(OH)_2$ refined using P-3m1 symmetric unit cell is shown in Fig. 4.11 and the structural parameters are presented in Table 4.4. Good refinement and

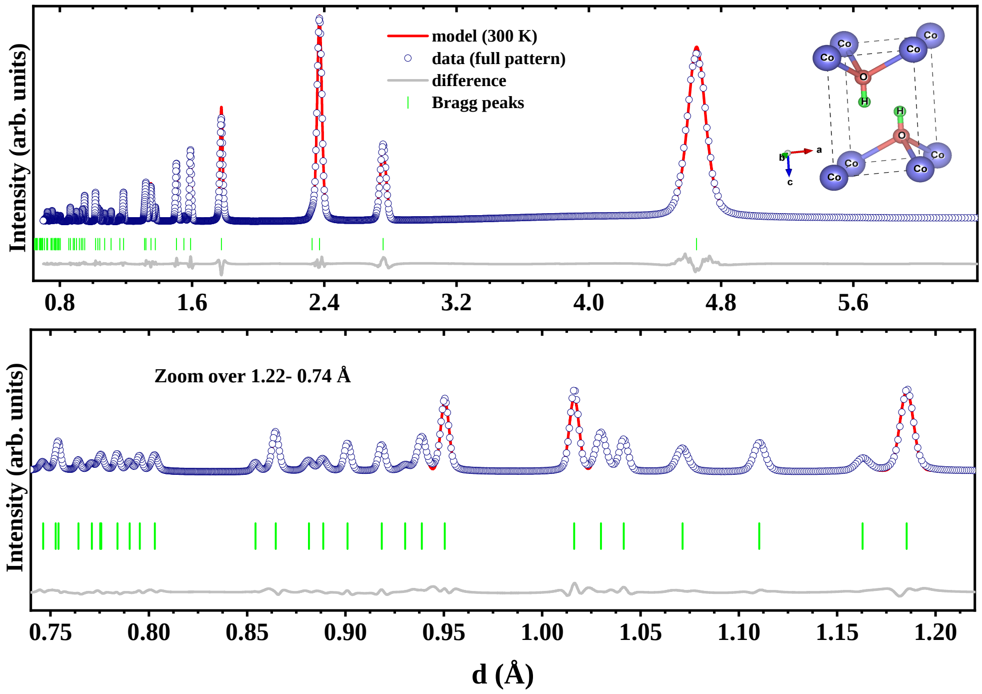

Figure 4.11: (a) Rietveld refinement of XRPD data of β-$Co(OH)_2$ at 300 K using P-3m1 symmetric unit-cell (see inset). Red solid lines and circles represents calculated patterns and measured data respectively. Bragg peak positions are indicated in green vertical bars. 'diff' represents the difference in measure and fitted curves. (b) A zoomed view of 0.74 – 1.22 Å which shows good agreement between the XRPD data and P-3m1 model.

reasonable agreement of structural parameters with the reported data validates the initial step of this high-pressure study. The high-pressure XRPD data of β-$Co(OH)_2$ up to 7 GPa using 4:1 methanol-ethanol mixture as PTM is shown in Fig. 4.12. Since refinement of the hydrogen atom is not possible due to its reduced cross-section towards X-ray, we conclude that, the Co-O lattice preserves the P-3m1 symmetry of β-$Co(OH)_2$ consistent with previous high-pressure studies. [111, 124, 132, 153, 157–159]. Even though the major peaks show gradual shifting with pressure, the minor peaks (013) and (003) were shown to behave abnormally around 2 GPa. The anomalous behaviour of (013) and (003) peaks is

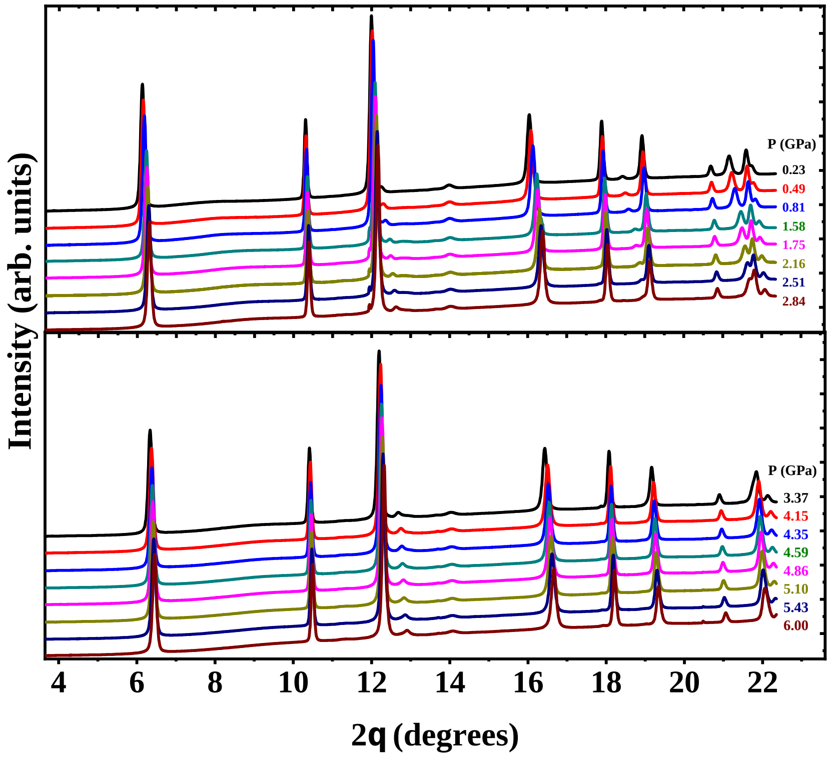

Figure 4.12: XRPD pattern of β-$Co(OH)_2$ using. 4:1 methanol-ethanol mixture as a PTM.

Table 4.4: Unit-cell parameters and bulk modulus of β-$Co(OH)_2$ from our study in comparison with previously reported works

a	c	c/a	V	K_0	K'_0	Method	Ref
3.18	4.64	1.459	40.69	56.14	4	XRD	This work
3.11	4.62	1.485 (+1.78)	40.83	36.00	4	PBE+U	This work
3.06	4.37	1.428 (-2.12)	35.38	55.8	4	PBEsol+U	This work
3.09	4.27	1.382 (-5.28)	35.42			PBEsol	This work
3.21	4.73	1.473 (+0.96)	42.30			vdW-DF2	This work
3.21	4.69	1.46 (+0.07)	41.93			vdW-DF2	This work
				73.3			[153]
3.20	4.67	1.459					[155]
3.185	4.662			XRD			[156]
3.181	4.634			ND			
3.13	4.82			PBE			
3.12	4.80			PBE+U			

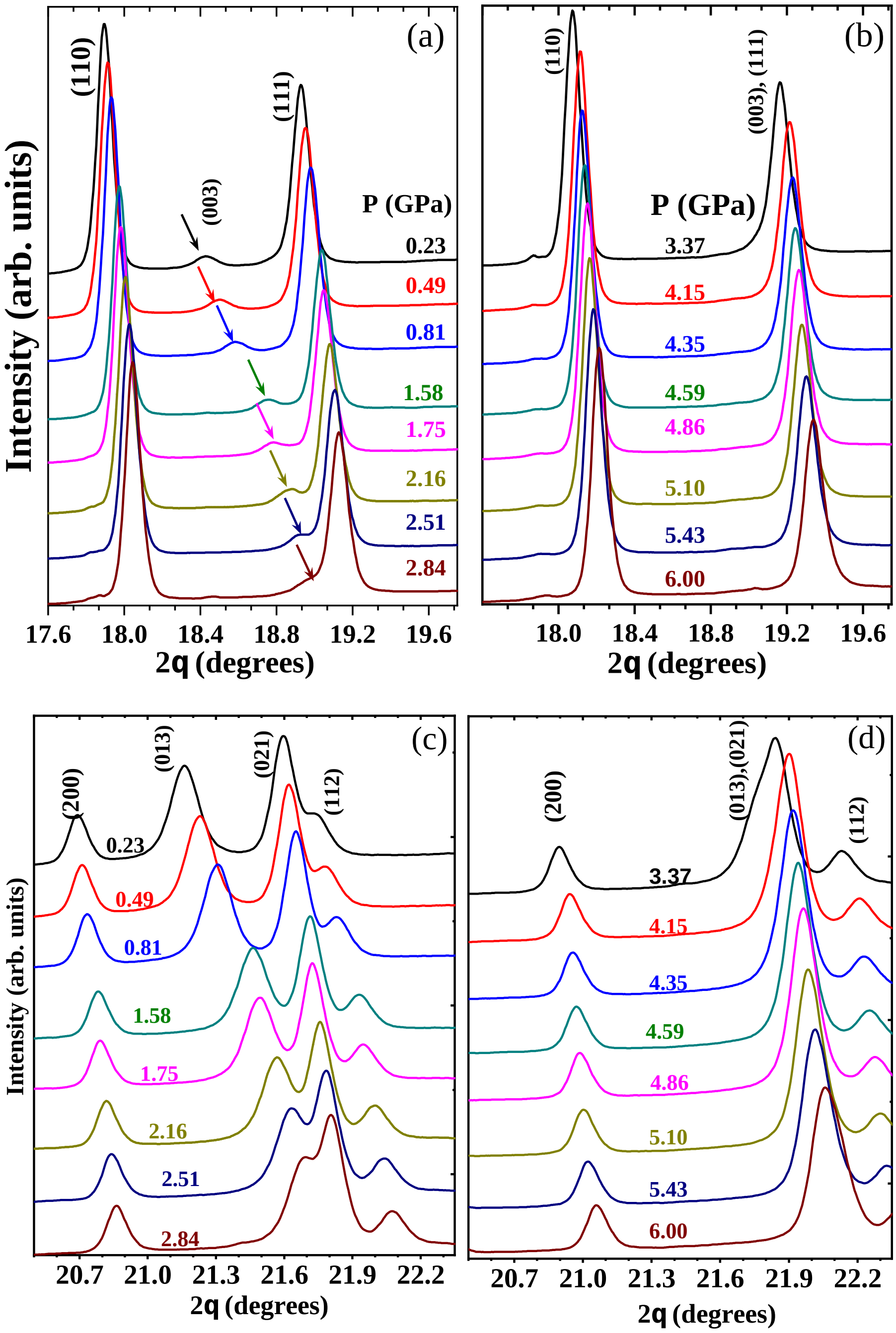

Figure 4.13: (a) and (b) shows a zoom over the (110), (003) and (111) peaks. (c) and (d) zoom over (200), (013), (021) and (112) Bragg peaks.

shown in Fig. 4.13 (a-b) and (c-d) respectively.The high-pressure data is divided into two panels for clear visibility of the changes in Bragg peaks. The high-pressure behaviour of (003) and (013) peaks shows that these peaks move relatively faster than other peaks and merges with their neighbouring peaks at 2.5 GPa. Due to subtle changes in diffraction pattern and lattice parameters it was inevitable to ensure the reproducibility of this

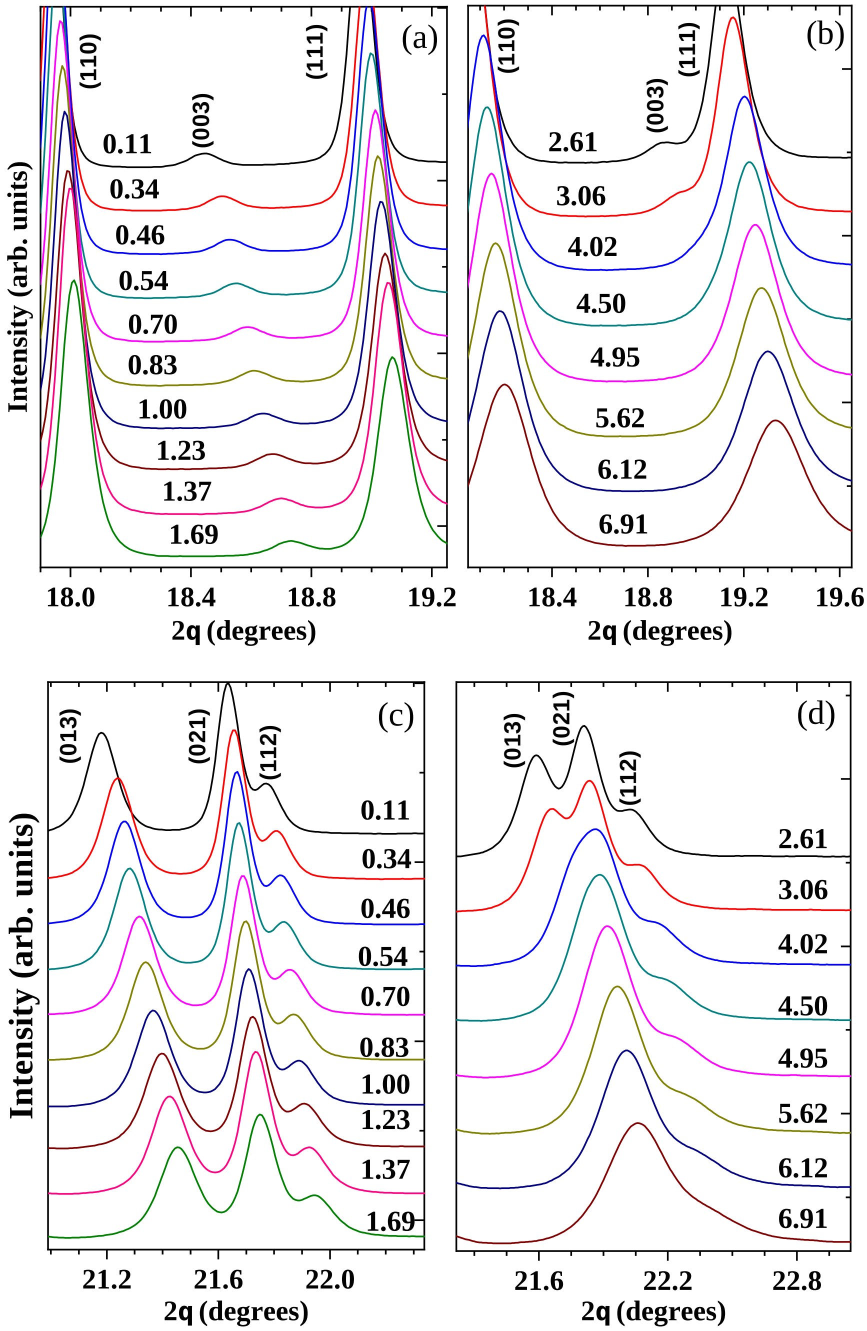

Figure 4.14: (a) and (b) shows diffraction pattern around (003) peak at all pressures in run 2 (silicone oil). (c) and (d) shows diffraction pattern around (013) peak at all pressures in run 2. In all the panels, numbers indicate the pressure values in GPa.

behaviour to discard the role of any non-hydrostaticity induced by the PTM. Another set of XRPD measurements on β-$Co(OH)_2$ were performed using silicone oil (SO) as PTM and the diffraction data is presented in Fig. 4.14. It is noteworthy that the anomalous behaviour of (013) and (003) peaks is reproduced in the second XRPD run confirming that the observed changes in diffraction peaks are intrinsic to the pressure response of the system. Unless specified, the following discussion on diffraction data refers to XRPD run using 4:1 methanol-ethanol mixture as PTM. The lattice plane corresponding to (003) peak lies parallel to the layer of hydrogen atoms whereas the plane corresponding to (013) peak itself is comprised of hydrogen atoms. Hence the anomalous behaviour of (013) and (003) peaks is governed by the charge distribution of hydrogen atom along (013) and (003) planes under pressure respectively. XRPD measurements couldn't refine the positions of hydrogen atom to evidence the rearrangement in hydrogen sublattice. Therefore, we performed electronic structure calculation to investigate the structural response of β-$Co(OH)_2$ under pressure. Similar to our DFT calculations on brucite (see Section 4.3.1), we adopted the $\sqrt{3} \times \sqrt{3} \times 1$ supercell proposed by Mookherjee, and Stixrude [111] to model the hydrogen disordered structure. Structural optimization of β-$Co(OH)_2$ was performed following a similar methodology adopted for studying the high-pressure behaviour of brucite as discussed in Section 4.3. At ambient condition, the β-$Co(OH)_2$ was shown to have P-3m1 symmetric structure with H--H distance of 2.03 Å which is lower than the vdW diameter of H (2.4 Å) thereby resulting in repulsive strain within the structure. Structural optimization showed that the β-$Co(OH)_2$ favours P-3m1 symmetry with hydrogen atom at 2d sites up to 5 GPa beyond which P-3 symmetric structure with hydrogen atom at 6i sites is energetically favourable. This indicates that β-$Co(OH)_2$ undergoes P-3m1 to P-3 transition at 5 GPa, higher than that observed in the case of brucite. To corroborate the DFT results with anomalous behaviour of diffraction peaks, the charge contour curves along the (003) plane were calculated corresponding to 0 and 5 GPa as shown in Fig. 4.15. At 0 GPa, the charge distribution along the (003) plane is characterised by circular contour curves whereas, the contours are distorted in nature for the hydrogen disordered P-3 symmetric structure. Hence, the anomalous behaviour of the Bragg peak at 2.5 GPa can be attributed to the hydrogen order-disorder transition in β-$Co(OH)_2$. The one to one correspondence between the occurrence of anomalies in Bragg peak and P-3m1 to P-3 transition in the same pressure regime is consistent with the result obtained in the study of brucite (see Section 4.3). Further, the hydrogen order-disorder transition in β-$Co(OH)_2$ at 2.5 GPa corroborates the reported Raman spectroscopic anomaly in FWHM of the $A_{1g}(2)$ mode around 2.5 GPa [154] (see Fig. 4.15)

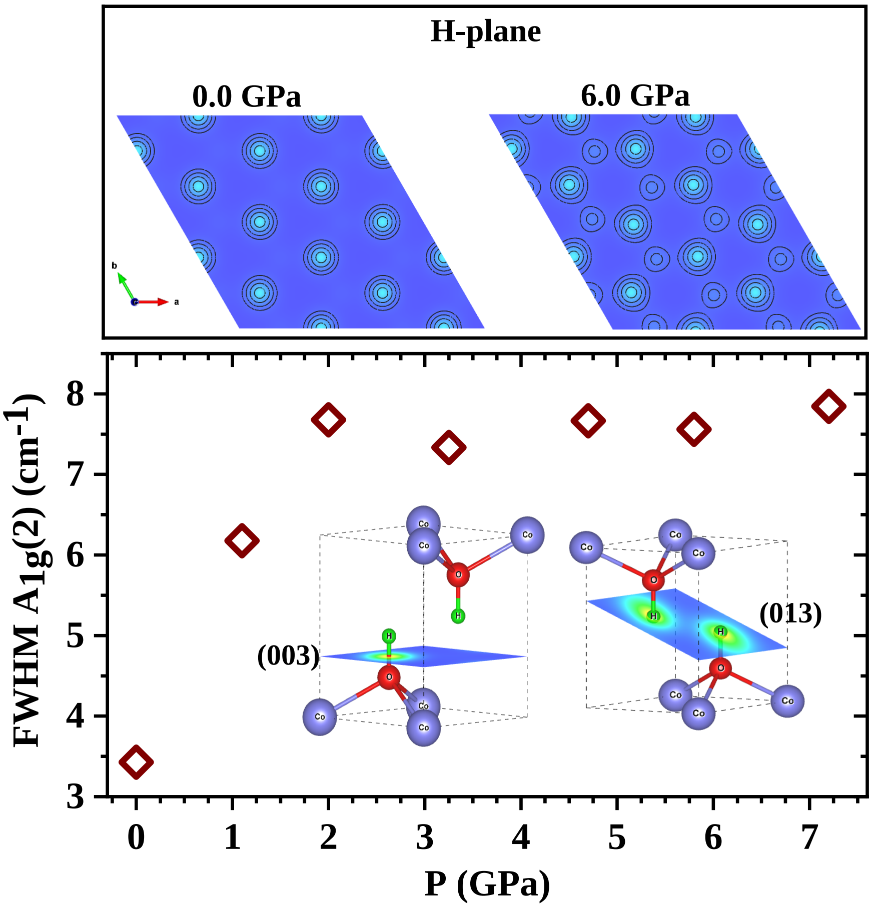

Figure 4.15: (Upper panel) Calculated charge density distribution along plane comprising of hydrogen atoms of β-$Co(OH)_2$ at 0 and 6 GPa. (Bottom panel) Reported pressure dependence of full width at half maximum of the $A_{1g}(2)$ mode [154]. Inset shows the corresponding eigen vectors and the charge density plot highlighting the role of hydrogen atoms on charge distribution along the (003) and (013) plane.

where the $A_{1g}(2)$ mode corresponds to the vibration of hydrogen atom parallel to the c axis as shown in the inset of Fig. 4.15. We therefore attribute the anomaly in A_{1g} (2) mode to the disordering of hydrogen atom in the crystal structure of β-$Co(OH)_2$.

To understand the effect of hydrogen order-disorder transition on unit-cell parameters of β-$Co(OH)_2$, the pressure dependence of lattice parameter and the ratio of the out-of-plane to in-plane lattice parameters (c/a) is shown in Fig. 4.16(a-b). It can be seen that the c/a ratio varies linearly with pressure above 2.5 GPa, i.e., in the hydrogen disordered structure. This can be attributed to the decrease in compressibility of the c -axis due to increases in H--H repulsion. The P-3m1 to P-3 transition enables to divide the studied pressure regime into two, that can describe the P-V data using two 2nd order

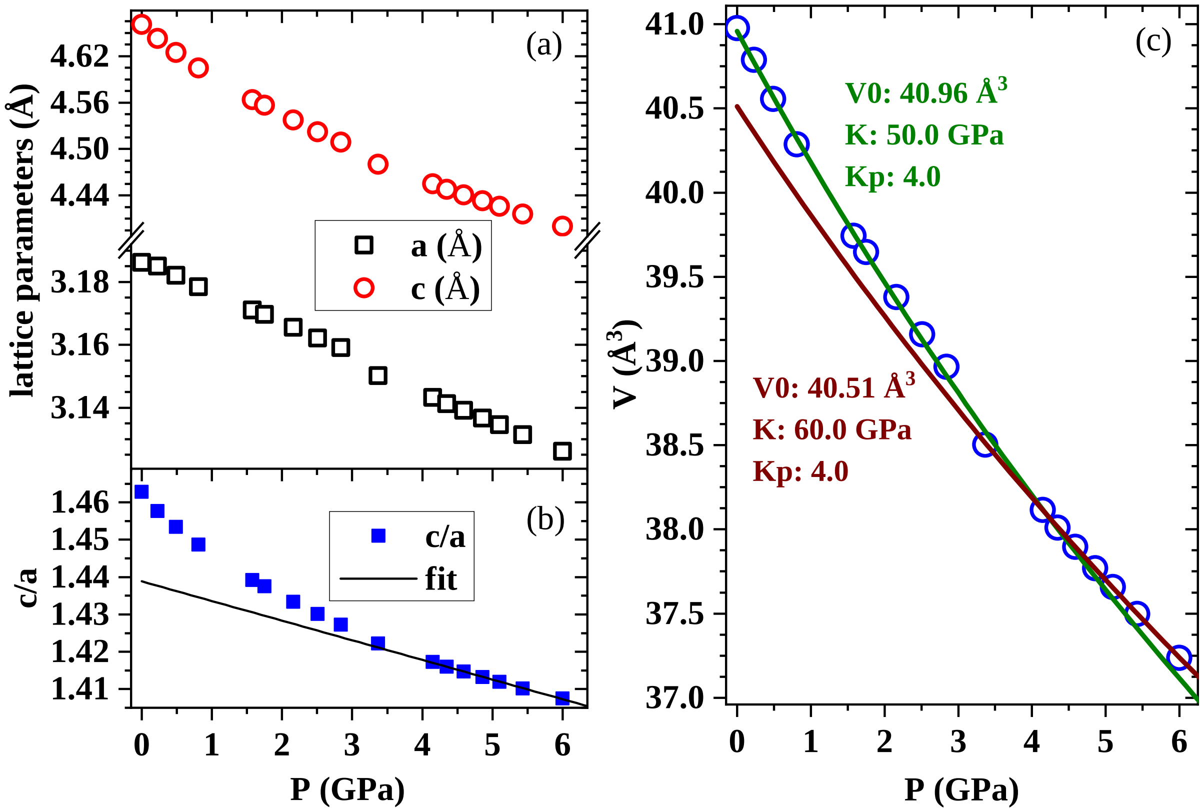

Figure 4.16: Pressure dependence of (a) experimental lattice parameters of β-$Co(OH)_2$ with pressure. (b) c/a-ratio and (c) unit-cell volume (circles). Green and brown lines are the 2nd order Birch-Murnaghan equation of fit with fixed Kp (=4).

Birch-Murnaghan equation of state with fixed derivative of bulk modulus (K_p=4) as shown in Fig. 4.16(c). The equation of state (EoS) fitting for low- and high-pressure phases yield bulk modulus of 50 and 60 GPa respectively. An increase in bulk modulus above 2.5 GPa suggests that the β-$Co(OH)_2$ becomes less compressible, which corroborates with pressure induced increase in H--H repulsion along c axis thereby opposing the compression mechanism along the c axis which is further consistent with the linear dependence of c/a on pressure across the transition.

4.5 Hydrogen order-disorder transition in β-$Ni(OH)_2$

Nickel hydroxides are widely studied for their potential applications in electrochemical sensors [160], photocatalysis [161], electronic devices [162], supercapacitors [163] and so on. There are two phases of nickel hydroxide: α- and β- $Ni(OH)_2$, among which β- $Ni(OH)_2$ is isostructural to brucite, having a trigonal structure with P-3m1 space group at ambient condition whereas α-$Ni(OH)_2$ consists of hydroxyl-deficient layers of β-$Ni(OH)_2$ that are intercalated by foreign anions and H_2O molecules [164]. Though β-$Ni(OH)_2$ has been subjected to crystallographic and spectroscopic investigations [154, 165–168], the high-pressure study on this material seeks attention. Similar to brucite and β-$Co(OH)_2$, the disordering of hydrogen and the corresponding transition pressure have not been addressed in the literature. Both hydrogen ordered and disordered models have shown to provide equivalent results for Rietveld analysis on neutron diffraction data of β-$Ni(OD)_2$ [169]. Interestingly, in their study, since the hydrogen order-disorder transition is inevitable in brucite like structure under large compression due to increase in H--H repulsion, absence of any anomalous behaviour in reported high-pressure XRD pattern [165] and Raman spectra [168] up to 10 and 25 GPa respectively made authors to conclude that the β-$Ni(OH)_2$ remains at hydrogen disordered structure even at ambient condition. However, a recent study on pressure dependence of Raman spectrum of β-$Ni(OH)_2$ reported an anomaly in full width at half maximum (FWHM) of modes associated with O-H bond of β-$Ni(OH)_2$ at a pressure around 4-5 GPa, similar to their observation for β-$Co(OH)_2$ at 2 GPa [154]. Our combined first principles and Raman spectroscopic study on β-$Co(OH)_2$ (Section 4.4) showed that the anomalous behaviour of O-H stretching modes for β-$Co(OH)_2$ is attributed to the hydrogen order-disorder transition. The structural similarity predisposes β-$Ni(OH)_2$ to behave similar to the β-$Co(OH)_2$. However, no conclusive evidence were reported for the structural anomaly in β-$Ni(OH)_2$ at such lower pressure regime. In this work, the pressure dependence of structural behaviour of β-$Ni(OH)_2$ using combined DFT and synchrotron XRPD measurements were studied. Similar to the investigation of β-$Co(OH)_2$, we analysed the changes in XRPD pattern to the structural properties obtained from DFT calculations and corroborated the results with the reported Raman spectroscopic measurement [154].

4.5.1 Results and Discussion

The ambient condition XRPD pattern refined using P-$3m1$ symmetric unit cell is shown in Fig. 4.17. Good refinement and better agreement of structural parameters with reported data (Table 4.5) validate the starting point of our high-pressure study. The diffraction

Table 4.5: Experimental and theoretical lattice parameters of β-$Ni(OH)_2$ in comparison with reported data.

a	c	c/a	Method	Ref
3.13	4.61	1.47	Expt. (300 K)	This work
3.28	4.66	1.42	DFT	This work
3.11	4.64	1.49	Expt	[168]
3.12	4.60	1.47	Expt	[170]
3.14	4.61	1.47	Expt	[165]
3.13	4.63	1.48	Expt	[171]
3.22 3.10	4.77 4.26	1.48 1.37	DFT	[171]
3.17	4.66	1.47	DFT	[172]
312 3.15	4.14 4.45	1.33 1.41	DFT	[173]

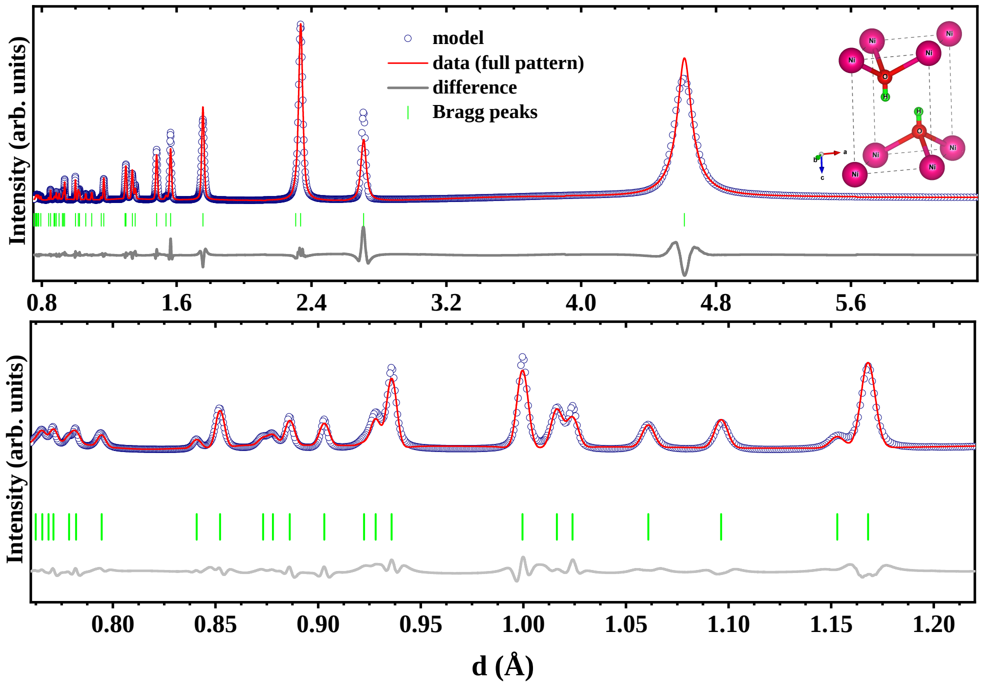

Figure 4.17: (Uper panel) (a) Rietveld refinement of XRPD data of β-$Ni(OH)_2$ at 300 K. (Inset shows P-3m1 symmetric unit cell used for refinement). Red solid lines and circles represents calculated patterns and measured data respectively. Bragg peak positions are indicated in green vertical bars. (b) A zoomed view of 0.76 – 1.22 Å which shows good agreement between the XRPD data and P-3m1 model.

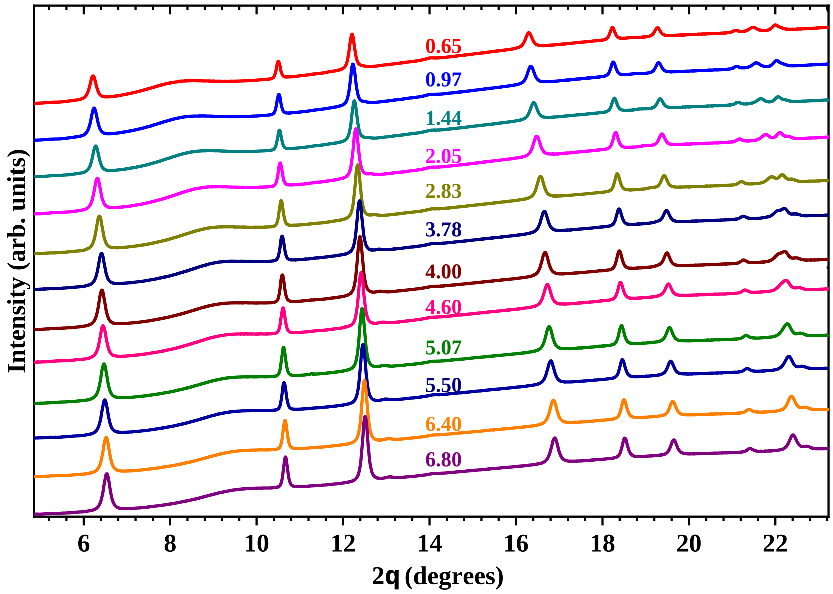

Figure 4.18: Measured synchrotron X-ray powder diffraction pattern of β-$Ni(OH)_2$ at high pressures.

pattern of β-$Ni(OH)_2$ at pressure up to 8 GPa is shown in Fig. 4.18. Good agreement with the refinement model and the XRPD data shows that the underlying symmetry of the lattice without considering hydrogen atom, due to its low cross-section for X-rays, is preserved to be P-$3m1$. Similar to high-pressure behaviour of XRPD pattern in β-$Co(OH)_2$, anomalous behaviour of (003) and (013) peaks was observed in XRPD pattern of β-$Ni(OH)_2$. The anomalous behaviour of the (003) peak is shown in Fig. 4.19 (a) where it shifts relatively faster towards a higher angle and merges with the neighbouring peak above 5 GPa. To confirm the observed anomaly in the diffraction pattern, another high-pressure run using silicone oil as PTM was performed. Analysis of (003) peak in latter run showed identical behaviour of merging with its neighbouring peak above 5 GPa, as observed with 4:1 methanol-ethanol as PTM (see Fig.4.19(b)) The reproducibility confirms that the structural anomaly in XRD peaks are the real response of the sample under study and thus, rules out any experimental artifact. The high-pressure behaviour of anomalously behaving peaks in β-$Ni(OH)_2$ can be compared with that obtained for β-$Co(OH)_2$.

Figure. 4.20 displays the intensity profile and interplanar spacing of (013) peak for both β-$Ni(OH)_2$ and β-$Co(OH)_2$ with pressure. Similar to that in β-$Co(OH)_2$, the d-spacing of (013) peaks decreases faster with pressure and merges with its neighbouring peak.

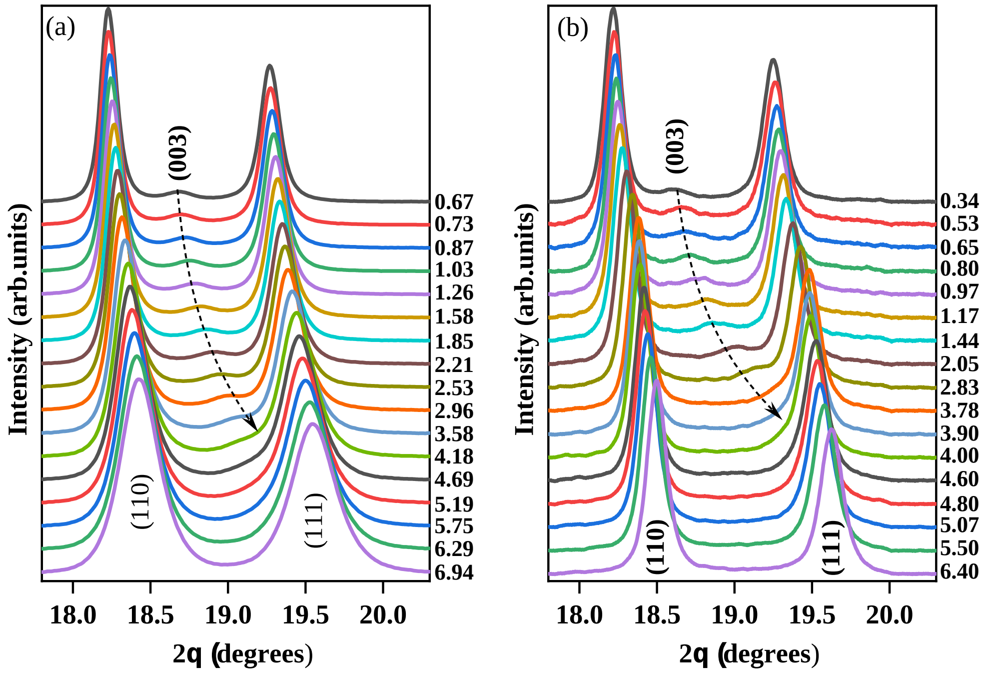

Figure 4.19: Measured XRPD data of behaviour of (003) diffraction peaks using (a) 4:1 methanol-ethanol mixture and (b) silicone oil as PTM.

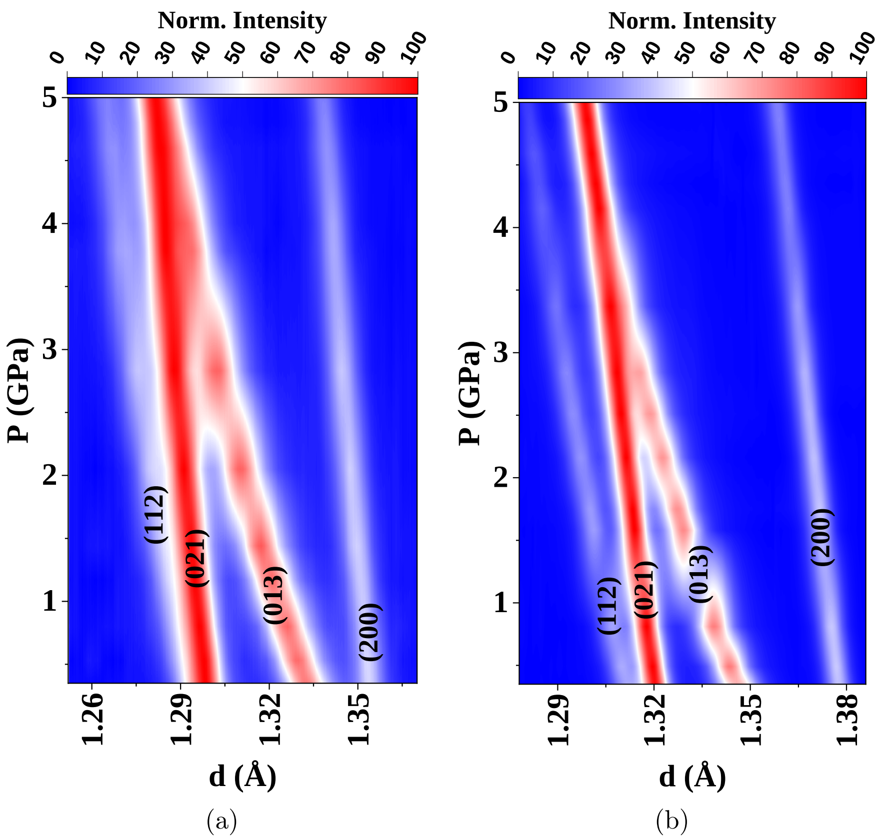

Figure 4.20: Intensity profile and pressure dependence of interplanar spacing corresponding to Bragg peaks in the neighbourhood of (013) peak of (a) β-$Ni(OH)_2$ and (b) β-$Co(OH)_2$.

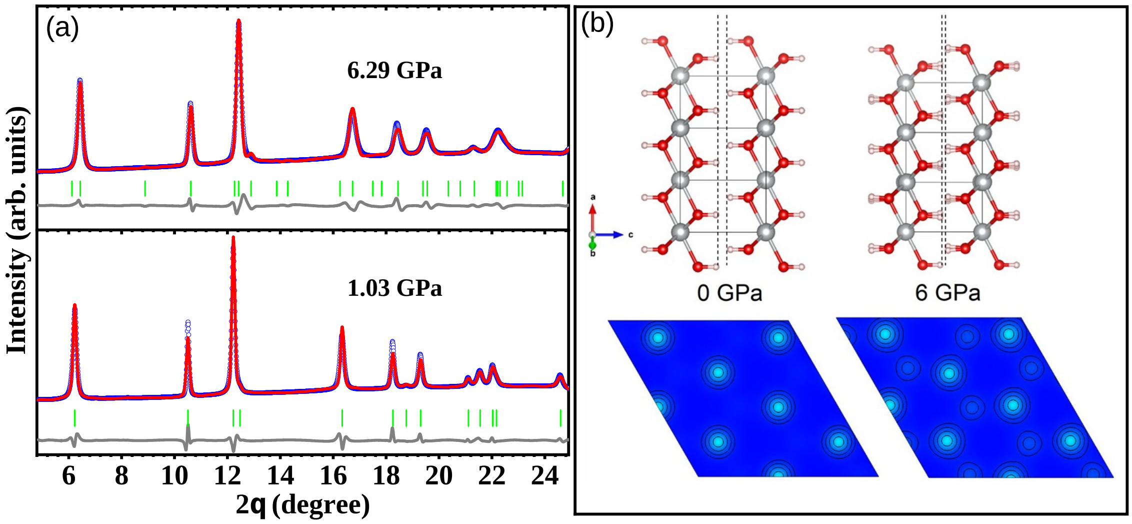

Figure 4.21: (a) Rietveld refinement of diffraction data of β-$Ni(OH)_2$ at low (lower panel) and high (upper panel) pressure regime fitted using P-3m1 and P-3 unit cell of β-$Ni(OH)_2$ respectively. (b) Optimised crystal structure (Upper panel) and calculated charge density distribution along H-plane (lower panel) of β-$Ni(OH)_2$ at 0 and 6 GPa respectively.

Following the high-pressure study of β-$Co(OH)_2$ discussed in 4.4.1, it is evident that the sudden variation in charge density distribution due to rearrangement of hydrogen atom along (003) and (013) plane is responsible for the anomalous behaviour of their corresponding Bragg peaks. The results are consistent with extended X-ray absorption fine structure (EXAFS) analysis by Marini et al. [166] where the rearrangement in H sublattice under pressure was proposed for β-$Ni(OH)_2$ with Ni-O sublattice being least affected. Structural optimization of $\sqrt{3} \times \sqrt{3} \times 1$ supercell of at various pressures showed that the β-$Ni(OH)_2$ exhibits P-3m1 symmetry up to 5 GPa above which the hydrogen atoms are displaced to 6i Wyckoff position reducing the symmetry to P-3. The refinement of XRPD data below and above 5 GPa with P-3m1 and P-3 symmetric model respectively is shown in Fig. 4.21(a). Above 5 GPa, the interlayer spacing is small enough to cause hydrogen disordering due to increased H--H repulsion which forces the axis of the hydroxyl group to deflect away from its initial direction (see upper panel of 4.21(b)). The relative positions of Ni and O atoms are retained up to 7 GPa preserving the initial symmetry of the Ni-O sublattice. This is consistent with the normal behaviour of (100) and (001) peaks observed in the XRPD pattern. To corroborate the anomalous behaviour of XRPD peaks, the calculated charge density along (003) plane is shown in Fig. 4.21(b). The

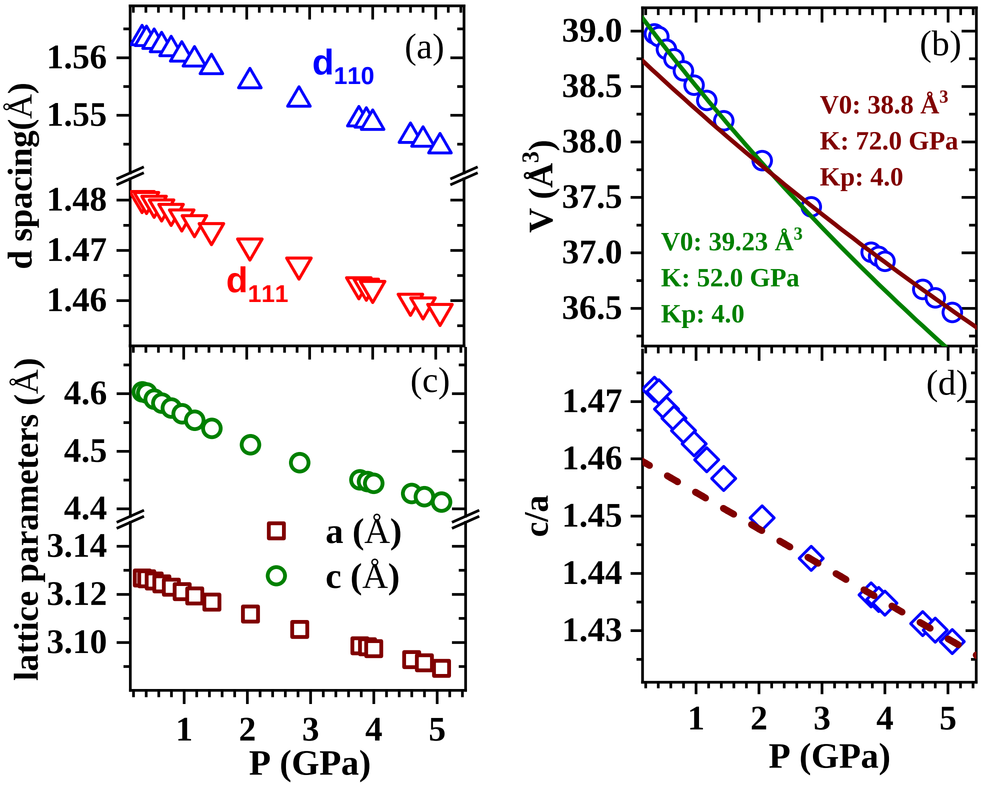

Figure 4.22: (a) Evolution of the d-spacing corresponding to (111) and (110) Bragg peaks of β-$Ni(OH)_2$. (b) Unit-cell volume (symbols) with pressure. Green and brown lines are the 2ndorder Birch-Murnaghan equation of state (Kp=4). (c) Change in experimental lattice parameters with pressure. (d) Variation in c/a-ratio with pressure. The linear fit of c/a above 3 GPa is shown by dotted line.

circular contour curves of charge density distribution undergo distortion above 5 GPa due to hydrogen disordering. The large variation in charge density distribution along (003) and (013) lattice plane attribute the anomalous behaviour of their corresponding Bragg peaks to hydrogen order-disorder transition.

The P-3m1 to P-3 transition in β-$Ni(OH)_2$ enables to divide the P-V data into two, corresponding to the low and high-pressure phases of β-$Ni(OH)_2$. Each phase is therefore conveniently described using 2nd order Birch Murnaghan equation of state. The bulk modulus of P-3 phase is 38.5% higher than that for P-3m1 phase. Higher bulk modulus indicates that the compressibility of β-$Ni(OH)_2$ decreases on hydrogen disordering. Fig. 4.22 shows the pressure dependence of c/a ratio. Initially, the c-axis is more compressible whereas at high-pressures, it behaves linearly with pressure indicating a less compressive c-axis. This is attributed to the increase in H--H repulsion as interlayer separation decreases with pressure, which resists further compression along the c-axis. The results are consistent with the anomalous behaviour of FWHM of the O-H stretching modes for β-$Ni(OH)_2$ reported by Marini et al. [154] (see Fig. 4.23) where two pressure regions can be identified. Inset of Fig. 4.23 shows the vibration of hydrogen atoms parallel to the *c*-axis corresponding to $A_{1g}(2)$ mode. Following the conclusion of study on β-$Co(OH)_2$(see Section 4.4.1), the one to one correspondence between P-3m1 to P-3 transition confirmed from DFT calculation and the observed anomaly in XRPD data around 5 GPa attributes the Raman spectral anomaly of β-$Ni(OH)_2$ to hydrogen order-disorder transition. The similarity between the behaviour of isostructural compounds : $Mg(OH)_2$, β-$Co(OH)_2$ and β-$Ni(OH)_2$ under pressure, attributes the structural anomaly owing to hydrogen order-disorder transition as a general characteristic of $M(OH)_2$ family of compounds.

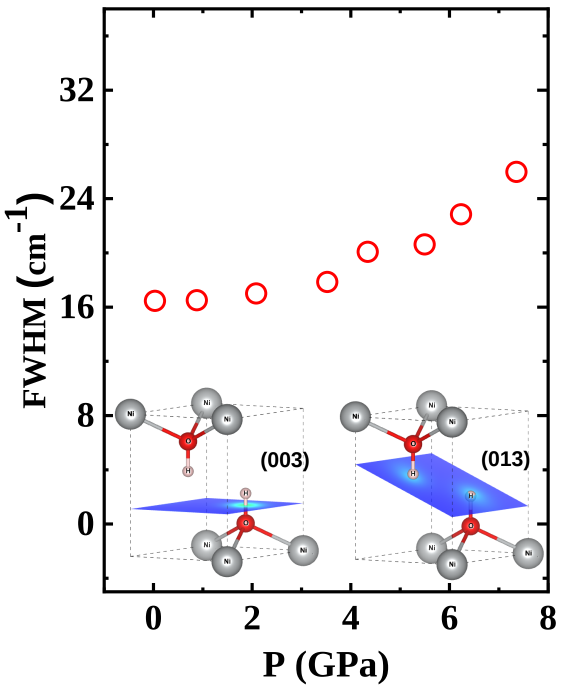

Figure 4.23: Reported pressure dependence of the FWHM of the $A_{1g}(2)$ mode from Ref. [154]. Inset shows the O-H vibrations corresponding to $A_{1g}(2)$ mode and the charge density plot showing the role of hydrogen atom in charge distribution along (003) and (013) plane of β-$Ni(OH)_2$.

4.6 Conclusions

The pressure response of $Mg(OH)_2$, β-$Co(OH)_2$ and β-$Ni(OH)_2$ has been studied using synchrotron XRPD and DFT based first principles calculations. For the brucite ($Mg(OH)_2$), we initially solved the existing discrepancy between previous experimental and theoretical studies on determining the preferred site for hydrogen atoms and thereby the lattice symmetry at ambient condition. The hydrogen disordered states for these three systems were simulated using $\sqrt{3} \times \sqrt{3} \times 1$ super-cell model. The geometrical optimization using various approximations to exchange-correlational functionals showed that the incorporation of van der Waals (vdW) interaction through a non-empirical vdW functional confirms the instability of P-3 over P-3m1 unit-cell of brucite at 0 GPa. The mechanical and lattice dynamical stability of P-3m1 structure was confirmed by Born stability criteria and real frequencies of phonon dispersion curves respectively. DFT calculations showed that the brucite undergoes hydrogen order-disorder transition under 1.38% of volume compression where the symmetry of brucite reduces to P-3. The structural changes under volume perturbation were studied using synchrotron XRPD measurements at low temperatures where the diffraction pattern was analysed from 100-400 K. The lowering of temperature to 100 K corresponds to pressure of 0.2 GPa due to thermal contraction. Diffraction data showed that the Bragg peaks corresponding to the crystallographic planes of hydrogen atoms behaves anomalously relative to other peaks and merges with neighbouring peaks below 150 K. This is attributed to the observed hydrogen order-disorder transition from DFT calculations.

The anomalous behaviour of diffraction peaks corresponding to hydrogen sublattice served as a probing tool for capturing hydrogen order-disorder transition. The similar methodology was adopted to study the pressure induced behaviour of hydrogen sublattice in β-$Co(OH)_2$ and β-$Ni(OH)_2$. High-pressure synchrotron XRPD analysis showed that the (003) and (013) Bragg peak, that corresponds to crystallographic plane consisting of hydrogen atoms, shows anomalous behaviour at 2.5 and 5 GPa for of β-$Co(OH)_2$ and β-$Ni(OH)_2$respectively where the peak moves relatively faster relative to other major Bragg peaks and merges with the neighbouring peaks similar to that observed in case of brucite. To rule out the contribution of non hydrostaticity induced by the PTM, if any, a 2nd high-pressure run was performed on both β-$Co(OH)_2$ and β-$Ni(OH)_2$ using silicone oil as PTM. DFT calculations on β-$Co(OH)_2$ and β-$Ni(OH)_2$ at high-pressure showed that the hydrogen atom prefers 6i sites at 2.5 and 5 GPa for $Co(OH)_2$ and β-$Ni(OH)_2$ respectively which corroborates the XRPD results. The charge density calculation evidences re-distribution of electronic charge along the H-plane across the hydrogen order-disorder transition pressure for both β-$Co(OH)_2$ and β-$Ni(OH)_2$. Further, our results explains the reported anomaly in pressure dependence of FWHM of $A_{1g}(2)$ mode for β-$Co(OH)_2$ and β-$Ni(OH)_2$ [154]. Consistent behaviour of Bragg peaks corresponding to plane comprising of hydrogen atoms were observed across hydrogen order-disorder transition for all the studied $M(OH)_2$ (M=Mg,Co and Ni) compounds. This shows that the synchrotron XRPD measurements combined with DFT based calculations can probe the pressure response of hydrogen sublattice. The study further showed that the hydrogen order-disorder transition owing to increased H--H repulsion under pressure is a common characteristic of brucite like structures.